Proceedings of the 1st Global Power and Propulsion Forum
GPPF 2017
Jan 16-18, 2017, Zurich, Switzerland
www.pps.global

GPPF-2017-77

# EFFECT OF HOLES ARRANGEMENT ON HEAT TRANSFER IN IMPINGEMENT/EFFUSION COOLING DOUBLE WALL SCHEMES

**Lorenzo Cocchi*, Alessio Picchi, Lorenzo Mazzei, Antonio Andreini**

**Department of Industrial Engineering Florence - DIEF**
**University of Florence**
*lorenzo.cocchi@htc.de.unifi.it
via S.Marta 3, 50139, Firenze, Italy

**Lorenzo Bellocci**

**Combustor Aero-Thermal Engineering**
**GE Avio S.r.l.**
lorenzo.bellocci@avioaero.it
via Primo Maggio 56, 10040, Rivalta di Torino (TO), Italy

## ABSTRACT

In the present work, two different impingement/effusion geometries have been investigated, with staggered hole configuration and equal number of impingement and effusion holes. The first geometry presents impingement hole pitch-to-diameter ratios of 10.5 in both the orthogonal directions and jet-to-target plate spacing of 6.5 hole diameters, with effusion holes inclined of 20° with respect to the target surface. The second geometry shows impingement hole pitch-to-diameter ratios of 3.0 in both the orthogonal directions, jet-to-target plate spacing of 2.5 diameters and normal effusion holes. For each geometry, two relative arrangements between impingement and effusion holes have been investigated, as well as various Reynolds numbers for the sparser geometry.

The experimental investigation has been performed by applying a transient technique, using narrow band thermochromic liquid crystals (TLCs) for surface temperature measurement. A CFD analysis has also been performed in order to provide a complete comprehension of the phenomena.

Results show unique heat transfer patterns for every investigated geometry. Weak jet-jet interactions have been recorded for the sparser array geometry, while intense secondary peaks and a complex heat transfer pattern are present for the denser one, which is also strongly influenced by the presence and position of effusion holes. For both the geometries effusion holes increase heat transfer with respect to impingement-only, which has been mainly attributed to a reduction in flow recirculation for the sparser geometry and to the suppression of spent coolant flow for the denser one.

## INTRODUCTION

Gas turbine development is characterized by a trend towards the increase in turbine inlet temperature, which is beneficial for the efficiency and power output of the engine. The main drawback of such trend is the ever increasing thermal load on all the engine components that are exposed to the hot gas flow: to sort out this issue, cooling systems have been developed, with the aim of keeping material temperatures to a level that ensures an adequate lifespan of hardware. In modern gas turbines, many different cooling techniques are applied together, and the interaction between various systems can strongly modify the performances of the single ones: accordingly, a study of the complete cooling configuration is often required to determine its performances. A highly effective cooling system, widely used in combustor liners and nozzle guide vanes, is the combination of impingement and effusion cooling: an array of coolant jets is generated by a perforated baffle and cools down the side of the wall opposite to the hot gas path; the spent coolant then enters an array of effusion holes in the wall itself and is evacuated at the opposite side, creating a protective film layer. The area averaged heat transfer coefficient (HTC) values on the cold side of the target wall can be up to 55% higher than the ones obtained with impingement alone (Cho and Goldstein [1]), and up to 10 times the values of effusion only (Cho and Rhee [2]). Heat transfer enhancement with respect to impingement alone is primarily attributed to the suppression of spent coolant flow (crossflow), which deflects coolant jets and degrades impingement performances (Cho and Goldstein [1], Rhee et al. [3]). Even so, the interaction between impingement and effusion flow fields can increase heat transfer even without crossflow, mainly thanks to the reduction of flow re-entrainment (Hollworth et al. [4], Rhee et al. [5]), while a minor role seems to be played by flow acceleration near the effusion holes (Hollworth et al. [4], Hollworth and Dagan [6]). The presence of impingement plate itself is also beneficial for hot gas side protection, since it allows to reduce the pressure drop across the effusion plate, thus decreasing the jet penetration (Meyers et al. [7]).

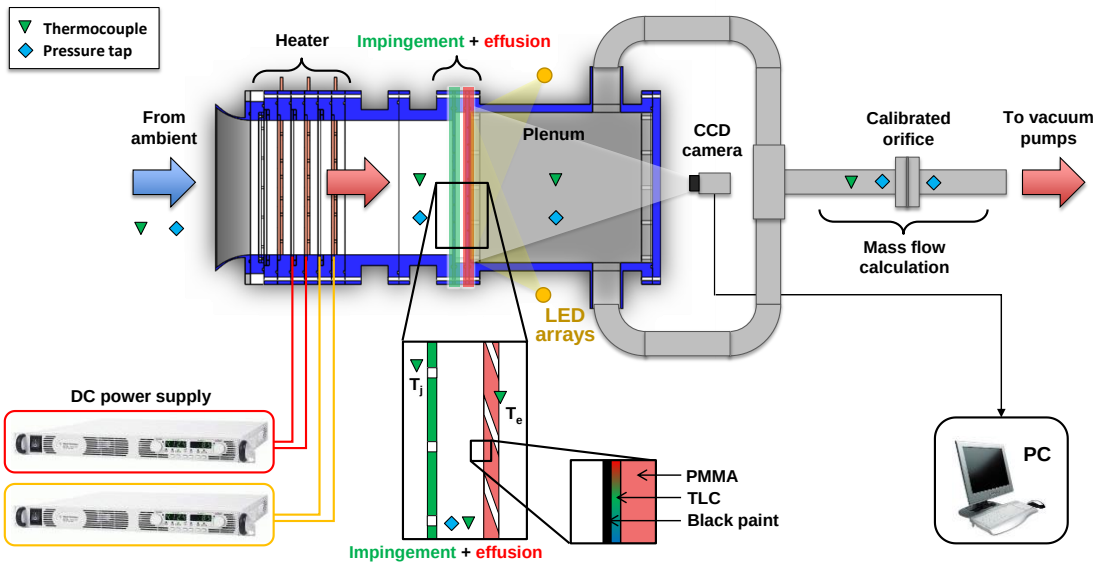


**Figure 1: Test rig scheme**

Given these considerations, it is evident that impingement/effusion cooling schemes represent a feasible strategy to increase cooling efficiency and save coolant. However, the implementation of such systems requires some aspects to be taken into account: in fact, cost and weight are superior if compared to simple effusion systems, and the maximization of cold side heat transfer may result detrimental in terms of hot side film effectiveness. As a consequence, each particular system requires a dedicated analysis to be performed.

The present work fits within such context, since it focuses on the measurement of HTC distribution on the effusion cold side of two distinct impingement/effusion systems presenting different geometric parameters. The effects of impingement and effusion arrays relative positioning, as well as of impingement jet Reynolds number, is experimentally investigated. The analysis of heat transfer distribution on the inner side of effusion plate is supported by CFD simulations: the combination of measured and calculated data allows to perform a complete analysis of thermal and fluid-dynamic phenomena, and thus to retrieve significant information on the peculiar behaviour of each geometry.

## EXPERIMENTAL ANALYSIS

### Experimental apparatus

Measurements were performed in the Heat Transfer and Combustion Laboratory of the Department of Industrial Engineering of the University of Florence (DIEF).

The test rig (depicted in Figure 1) consists of an open-loop, suction type wind tunnel, and is designed to replicate on an enlarged scale the thermal and fluid-dynamic phenomena involved by a combined impingement/effusion cooling system. The vacuum system is composed of four inverter controlled vacuum pumps, with a total maximum capacity of about 2400 $m^3/h$; they allow air at ambient pressure and temperature to be driven into the rig inlet section. Since a transient technique is used for heat transfer measurements, air needs to undergo a fast and uniform temperature change: as a consequence, the first component encountered by the air flow is a purpose built six stage mesh heater. The number of active stages is defined by the required thermal power. Electric power is provided to the stages with the help of dedicated DC power supplies. A straight PMMA duct connects the mesh heater to the cooling geometry model: the small length (200 mm) and the low thermal conductivity of the material (0.19 W/mK) allow to preserve the uniform temperature profile of the heated air flow.

The cooling geometry is also entirely made of transparent PMMA, thus allowing both thermal insulation and optical access to the inner surfaces. The impingement/effusion system is replicated by two parallel plates, housing the impingement (I) and effusion (E) holes arrays, and a spacer, built as a square frame, which separates the two plates and defines the impingement-to-target plate spacing.

Two main configurations have been investigated, which will be referred as Geometry 1 and 2: the corresponding impingement and effusion geometries will be indicated as I1 and E1 for the first Geometry and I2 and E2 for the second one. Each configuration presents the same number of impingement and effusion holes, arranged in staggered arrays. Geometric features of the two geometries are summarized in Table 1, namely impingement jet-to-jet spacings in both orthogonal directions x and y defined on the plate itself, X and Y, jet-to-target plate spacing Z, effusion hole diameter $D_e$, impingement and effusion plates thickness $S_i$ and $S_e$, all scaled with respect to the impingement hole diameter $D_i$. Holes axes inclinations with respect to the plates $\beta_i$ and $\beta_e$ are also reported, as well as the impingement and effusion holes number $N_i$ and $N_e$.

Heat transfer performances of an impingement/effusion cooling system also depend upon the relative position of impingement and effusion holes (Hollworth et al. [4], Hollworth and Dagan [6], Cho et al. [8]): to investigate such

**Table 1: Investigated systems geometric characteristics.**

| Geometry | $X/D_i$ [-] | $Y/D_i$ [-] | $Z/D_i$ [-] | $D_e/D_i$ [-] | $S_i/D_i$ [-] | $S_e/D_i$ [-] | $\beta_i$ [°] | $\beta_e$ [°] | $N_i$ [-] | $N_e$ [-] |
|---|---|---|---|---|---|---|---|---|---|---|
| 1 | 10.5 | 10.5 | 6.5 | 1 | 1.3 | 2 | 90 | 20 | 60 | 60 |
| 2 | 3.0 | 3.0 | 2.5 | 0.9 | 0.5 | 0.7 | 90 | 90 | 54 | 54 |

dependency, two different relative arrangements were examined for both Geometry 1 and 2: in the first arrangement, which will be referred as Assembly 1 (A1), impingement holes projections on the effusion plate lie midway the effusion holes in both orthogonal directions (i.e. the two arrays are shifted of ½ X in the x direction and ½ Y in the y direction); in the second arrangement, which will be named Assembly 2 (A2), the rows of impingement and effusion holes are aligned, but each hole is shifted of ½ Y in the y direction. Figure 2 summarizes the two proposed assemblies, showing the effusion and impingement hole traces on the effusion plate cold side.

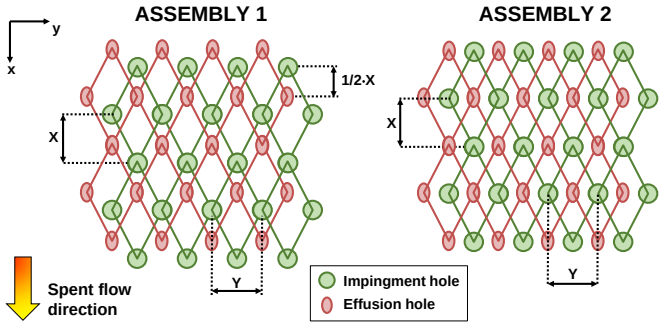


**Figure 2: Investigated holes relative positions.**

To assess the effect of coolant extraction through effusion holes, heat transfer from the impingement arrays of both geometries on a smooth target surface (E0) has also been investigated. In the latter case, coolant extraction is performed by means of two large slots, symmetrically located at the outer sides of the smooth target plate in the x direction, with 30×280 $mm^2$ rectangular cross section. This realization ensures the impingement flow field to be only altered by jet-jet interactions and spent coolant flow (crossflow), and provides an impingement-only reference case for each geometry.

A PMMA plenum with inner volume of 280×280×320 $mm^3$ is located downstream the effusion plate and collects the spent coolant flow, which is then extracted and directed towards the vacuum system.

The aim of this work is to determine heat transfer coefficient distributions on the effusion plate upstream surface (effusion cold side). According to the transient HTC measurement approach, the temperature distribution of such surface needs to be monitored during the test: to achieve this goal, narrow band thermochromic liquid crystals (TLCs) have been used; the employed TLC formulation is provided by LCR Hallcrest and has a colour play range between 40°C and 41°C. The target heat transfer surface has been sprayed first with the TLC coating, and then with a water base black paint, to provide the TLCs a non-reflecting background. TLCs colour (i.e. surface temperature) evolution is recorded by means of a Sony XCD-SX90CR CCD camera connected to a PC via IEEE 1394b interface. The camera is located outside of the plenum, and observes the heat transfer surface through the effusion plate itself and the rear side of the plenum, which is then designed as a transparent PMMA optical window. Illumination is provided by two 8 W white LED arrays, capable of 750-800 lumen each.

To ensure an accurate colour-temperature response, TLCs have been calibrated in the same optical conditions of the real test following the steady state gradient method (Chan et al. [9]): the effusion plate has been replaced with a PMMA sheet of the same thickness, sprayed with TLCs and black coating; the side not observed by the camera is thermally connected with a 4 mm thick, rectangular aluminium plate by means of heat transfer compound. A side of the plate is heated by a cartridge electrical heater, while the opposite side can be cooled through a flow of compressed air. The whole assembly is thermally insulated from the environment by an expanded polyurethane enclosing. The plate is designed in such a way that, by regulating the heating power and the air mass flow rate, a suitable one-dimensional temperature gradient can be set along the plate itself. Nine T type thermocouples (0.5 K measurement accuracy), whose locations are exactly known, measure the plate temperature in different locations, which can then be associated with the TLC colour response recorded by the camera. To improve accuracy in such a narrow temperature band, thermocouples have been recalibrated using a Pt100 RTD (uncertainty ±0.1, level of confidence 95%). In this case, a specific temperature needs to be associated with a precise event (as will be better explained in the next section): the most repeatable and evident effect resulted to be the green colour peak intensity, which has then been chosen as the colour descriptor. Calibration has been repeated several times in order to improve the reliability of the results. For the lot of TLCs used for the whole experimental campaign, the calibrations showed a mean value of the green peak at 40.5°C with a standard deviation of 0.13°C.

Local temperature measurements in different points of the rig is performed thanks to several T type thermocouples, connected to a data acquisition/switch unit (Agilent 34970A). In particular, such a measurement is needed to know air temperature evolution, requested by transient technique data reduction: as a consequence, a small thermal inertia is needed for the sensor in order to correctly describe temperature evolution. Air temperature is thus registered by thermocouples with 0.5 mm diameter sheath, directly located upstream the impingement holes: the combination of small sensor mass and high air velocity provides a maximum time constant of around

0.5 s for the thermocouples, which is considered satisfactory for the present case.

Local pressure measurements are performed thanks to a Scanivalve DSA 3217 pressure scanner, housing 16 piezoresistive relative pressure sensors with a maximum accuracy of 6.9 Pa. To ensure the desired flow conditions to be replicated, air mass flow rate is measured on the extraction line through a calibrated orifice, according to the standard EN ISO 5167-1. Mass flow rate is controlled by varying pump speeds.

## Experimental procedure

As mentioned above, heat transfer tests are performed using a TLC transient technique. The desired flow conditions are initially set by circulating ambient air into the rig, thus keeping the whole geometry at constant ambient temperature. When pressure and mass flow rate reach steady conditions, the camera starts recording (1280×960 resolution at 30 fps) and the mesh heater is turned on, thus causing air to undergo an as quick as possible temperature step (around 1.5 s to reach target temperature). The test ends when TLCs reach the maximum of green intensity in every point of the target surface.

The transient method for convective heat transfer coefficient $h$ calculation is based on transient heat transfer between a solid surface and a fluid when the latter undergoes an instantaneous temperature change (Ireland et al. [10], Camci [11]). Under the hypotheses of one-dimensional conduction and semi-infinite solid, surface temperature evolution is described by:

$$\frac{T_w(t)-T_{init}}{T_j-T_{init}} = 1 - \exp\left(\frac{h^2 \alpha t}{k^2}\right) \operatorname{erfc}\left(\frac{h\sqrt{\alpha t}}{k}\right) \quad (1)$$

where $T_w$ is the surface temperature, $T_{init}$ is the initial wall temperature, $T_j$ is the air temperature, $t$ is the time elapsed from air temperature change and $\alpha$ and $k$ are respectively thermal diffusivity and conductivity of the wall material (PMMA in the present case). If the time employed to reach the green peak intensity is known for every point of the TLC coated surface, as well as the temperature corresponding to such peak (thanks to TLC calibration), $h$ distribution can be calculated from equation 1. Since in the present case a quick, yet not instantaneous air temperature step could be realized, the principle of superimposition has been applied to model gas temperature profile in data reduction procedure. The semi-infinite solid hypothesis has been assessed by verifying the maximum test duration to be lower than the limit condition proposed in the study of Vogel and Weigand [12].

Flow conditions are identified by the impingement jet Reynolds number, defined as:

$$Re_j = \frac{\dot{m} D_i}{N_i A_i \mu} \quad (2)$$

where $\dot{m}$ is overall air mass flow rate, $A_i$ is the impingement hole cross-section and $\mu$ is air dynamic viscosity. Since target temperature establishes quickly after the beginning of the test and undergoes little variation during the test duration, air properties are calculated at the target temperature itself. Reynolds numbers ranging from around 2500 to 10000 have been investigated for Geometry 1, while Geometry 2 was tested at a single $Re_j$ value of around 15700. Convective heat transfer coefficient values have been reformulated in a dimensionless form as Nusselt number values, defined as:

$$Nu = \frac{hD_i}{k_j} \quad (3)$$

where $k_j$ is air thermal conductivity. For every test, the results in terms of Nusselt number distributions will be presented normalized as $Nu/Nu_0$, where $Nu_0$ is the Nusselt area averaged measured in the regions Row 1 (see Figure 5(a)) for the test configuration with the impingement plate I2 and smooth target surface (E0) at around $Re_j$=15700. Such a kind of normalization allows to appreciate the relative difference between the geometries and the relative impact of flow conditions.

## Experimental uncertainty

The uncertainty analysis has been performed according to the standard ANSI/ASME PTC 19.1 [13], based on the Kline and McClintock method [14]. A maximum uncertainty of 2.2% has been evaluated on $Re_j$, with typical values ranging from 1.5% to 2%. The same approach has been applied to the Nusselt number evaluation. Given the employed technique, the uncertainty on $Nu$ depends upon temperature measurement accuracy (both of TLCs and thermocouples), wall material properties and measurement sample rate (given by data acquisition and camera framerate). A typical distribution of measurement uncertainty on $Nu$ is reported in Figure 3.

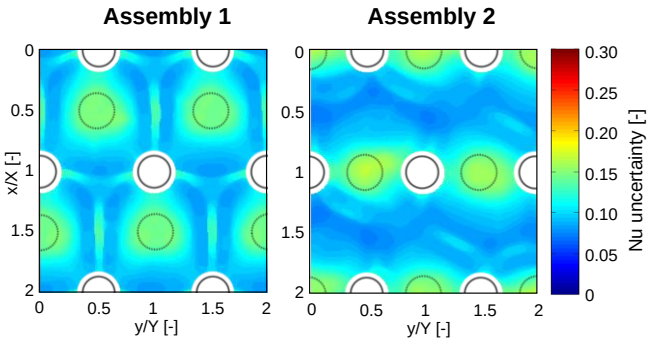


**Figure 3: Uncertainty distribution for Geometry 2 at around $Re_j$=15700**

As it can be observed, for local $Nu$ values, uncertainty can be as high as 20% where Nu peaks occur (due to the quick TLC colour play), while being below 10% in every other region. Maximum uncertainty on area averaged $Nu$ value is 12% (for Geometry 1, Assembly 1 test at around $Re_j$=7400), with typical values falling in the range of about 8-10%. All the reported uncertainties bounds are based on a 95% confidence level.

## NUMERICAL ANALYSIS

As a consequence of the employed experimental setup, heat transfer measurement is not possible or at least not reliable in some localized regions, e.g. in the zones covered by the Geometry 2 inclined effusion holes (due to limited optical access) and in the immediate proximity of effusion holes (due to unreliability of one-dimensional transient heat transfer

hypothesis). This issue suggests the opportunity to exploit CFD to have a better insight to the actual heat transfer distribution and flow field generated by the double wall system. At this purpose, steady RANS simulations were performed for the four impingement/effusion configurations.

A sketch of the computational domain for Geometry 1 (I1E1) is reported in Figure 4. The boundary conditions at the inlet were assigned in terms of mass flow rate and total temperature, whereas a static pressure condition was prescribed at the outlet: all the conditions are derived from the ones measured during experimental tests, chosen in order to match the average jet Reynolds number. All the walls were treated as smooth and adiabatic, with a no slip condition, except for the target plate, to which a constant temperature was imposed. The translational geometrical and fluid dynamic periodicity allows to reduce the computational effort considering only two rows in the streamwise direction and a further reduction is achieved imposing a symmetry condition in the lateral direction.

ANSYS Meshing was used to generate the computational grid depicted in Figure 4. A quite coarse sizing was used in the plena, whereas the mesh was refined in the proximity of the impingement jets, according to the results of a mesh sensitivity analysis (not reported for the sake of brevity). Approximately, fifteen elements per hole diameter were used to discretize the perforations. The hybrid unstructured mesh consists of tetrahedrons and a layer of 15 prisms included on the target plate to ensure a $y^+$ value around unity. As a result, computational grids with a total of 4.3-4.5·$10^6$ elements and 1.10-1.25·$10^6$ nodes were generated.

Steady RANS calculations were carried out using the Navier-Stokes solver ANSYS Fluent v16.2. The fluid was treated as an ideal gas with variable properties: thermal conductivity, dynamic viscosity and specific heat capacity at constant pressure are considered temperature-dependent. The second order upwind scheme was used to provide an accurate solution. Turbulence was treated using the k-ω SST turbulence model, which, according to Zuckerman and Lior [15] provides the most accurate results among two-equation eddy viscosity models. The Wall Integration treatment was recovered thanks to the cell clustering on the surfaces of interest.

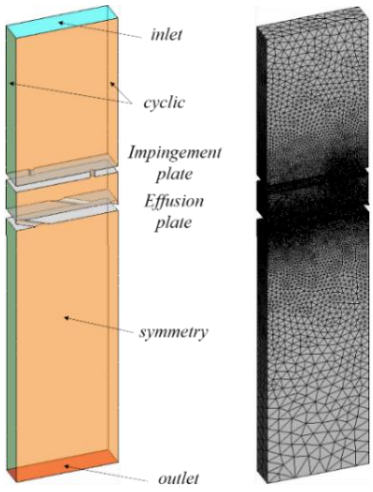


**Figure 4: Computational domain and grid.**

## RESULTS

### Results validation

The results presented in the following paragraphs are obtained from the first experimental campaign performed on the test rig described above: as a consequence, a fundamental step consists in the validation of the experimental data. To achieve such goal, the results obtained with impingement only configuration have been compared with the outcomes of impingement correlation available in the open literature. In particular, the configuration obtained combining impingement plate 2 (I2) with the smooth target surface (E0) presents geometric parameters which correspond to Bailey and Bunker [16] correlation validity ranges.

$Nu/Nu_0$ distribution for the test performed at around $Re_j$=15700 is reported in Figure 5(a) The two extraction slots (located above and below the surface presented in Figure 5(a)) cause a symmetric flow field to establish, which can be identified as generated by two equal, undisturbed impingement arrays. As a consequence, the experimental area averaged $Nu$ values reported in Figure 5(b) are obtained as the average of each couple of symmetric rows. The chart shows that the correlation only slightly overestimates measured values (differences ranging from 6.5% to 7.6%) and that the trend is also correctly replicated: as a consequence, a satisfactory agreement can be identified. The experimental procedure and apparatus employed in the present study can thus be considered validated.

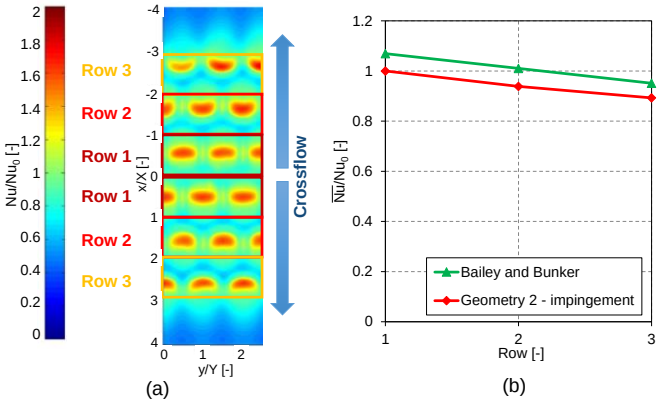


**Figure 5: $Nu/Nu_0$ distribution at around $Re_j$=15700 test (a) and comparison with Bailey and Bunker [16] correlation (b).**

### Geometry 1 results

Figure 6 reports $Nu/Nu_0$ distributions for Geometry 1 for the two hole assemblies, all obtained at $Re_j$=7400. Geometry 2 results will be presented separately in the following paragraphs, given the considerable differences between the two configurations. Maps report the effusion holes locations (solid lines) and the projections of impingement holes on the investigated surface (dashed lines). The areas surrounding the effusion holes (in which one-dimensional heat transfer hypothesis could be invalid) and the ones covered by the effusion holes traces are not reported.

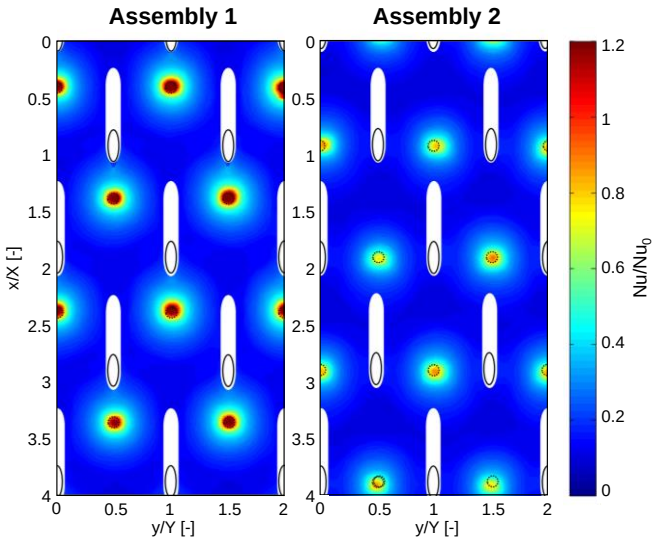


**Figure 6: *Nu/Nu₀* distributions for Geometry 1 (I1E1) at around *Re$_j$*=7400.**

Jet-jet interactions appear to be weak, mainly due to the relatively high jet-to-jet distance. The effect of impingement/effusion holes relative positioning can be appreciated by comparing the two maps of Figure 6, corresponding to the two investigated assemblies. The general shape of heat transfer pattern is similar for the two assemblies; however, a slight shift of the peak location towards the positive x direction can be identified for Assembly 2, as well as a less circular shape of the *Nu* distribution, which seems to be slightly enlarged towards the same positive x direction. Regarding *Nu* values, the entity of *Nu* peaks is significantly higher for Assembly 1, while far from the peaks and around the effusion holes only slight differences can be noticed.

Making references to Figure 7, CFD simulations reproduce with a reasonable agreement the pattern of the *Nu* contours, as well as their magnitude (discrepancies with experimental data range from 5% to 17%, according with the expected values for the exploited computational model [15]). This gives the opportunity to exploit the predictions to obtain a better understanding of flow physics within the system and its impact on heat transfer characteristics.

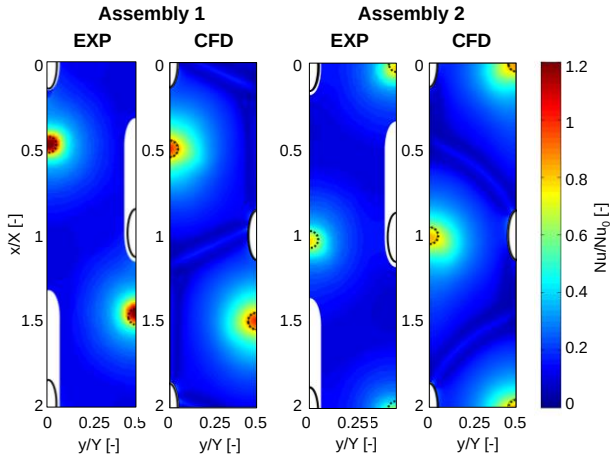


**Figure 7: *Nu/Nu₀* distributions for Geometry 1 (I1E1) at around *Re$_j$*=7400: comparison between experimental data and CFD simulations**

The predicted flow field reproduced by CFD on the left symmetry plane (y/Y=0) is depicted in Figure 8 that, in conjunction with the corresponding *Nu* map, allow to draw some interesting considerations. The different peak values of Nusselt number in the proximity of the stagnation region can be ascribed to the impingement/effusion pattern characteristic of each assembly. For the Assembly 1 the impingement jet appears to be approaching the target plate following a straight trajectory, an expected behaviour due to the absence of a dominant crossflow. Nevertheless, when the Assembly 2 is considered, the jet seems to be attracted by the preceding effusion row, leading the impingement jet to be bent towards the upstream direction. This phenomenon behaves similarly to crossflow, as confirmed by the kidney-shaped stagnation region (see for example Row 3 in Figure 5), hence justifying the detrimental impact on the cooling performance observed for the Assembly 2 configuration.

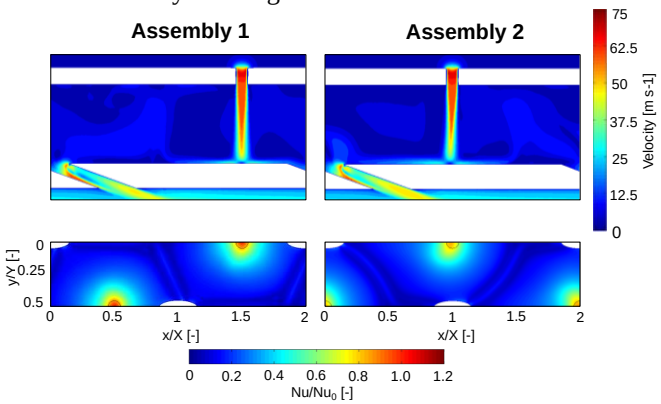


**Figure 8: Flow field predicted by CFD for Geometry 1 (I1E1) at around *Re$_j$*=7400**

*Effect of Reynolds number*

To assess the effect of different mass flow rates on impingement/effusion cooling performances, four tests were performed for each Geometry 1 assembly, thus to obtain *Re$_j$* values ranging from 2500 to 10000. The *Nu/Nu₀* distributions obtained for Assembly 2 are reported in Figure 9. It can be observed that the shape of heat transfer pattern is not significantly influenced by a variation of *Re$_j$* in the investigated range, while heat transfer is enhanced by an increase of *Re$_j$* in every point of the map. The same considerations can be derived for the Assembly 1 maps, which are not reported for the sake of brevity.

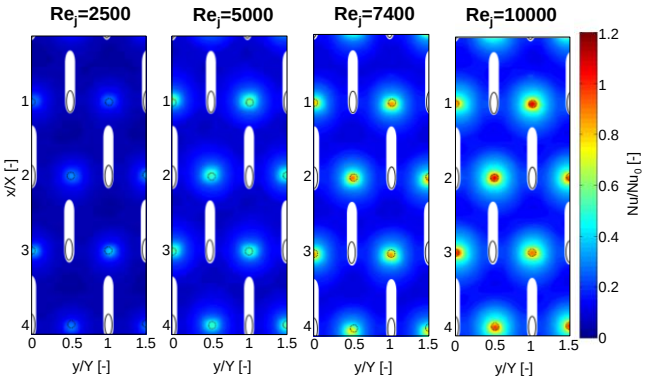


**Figure 9: *Nu/Nu₀* distributions for Geometry 1, Assembly 2 for different *Re$_j$* values.**

Given these results, significant conclusions can be drawn by comparing area averaged *Nu* values for the investigated cases, which is performed in Figure 10. It is evident that Assembly 1 outperforms Assembly 2 for the whole $Re_j$ range, which demonstrates the flow phenomena causing this difference to occur in every investigated condition. However, the relative differences decrease from 33% to 19% as $Re_j$ increases, and the power law fittings of the two data sets (solid lines) show a slightly stronger heat transfer enhancement of Assembly 2 as $Re_j$ grows. The latter fact seems to indicate that the detrimental effect of locally induced jet deflection verified for Assembly 2 is reduced if impingement jet momentum increases.

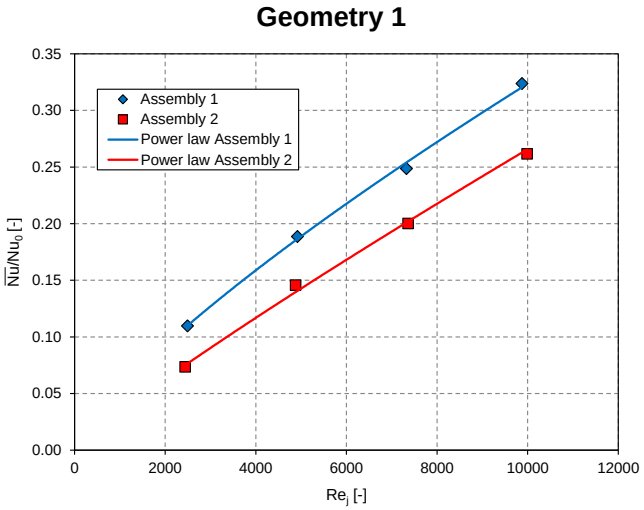


**Figure 10: Effect of $Re_j$ on area averaged *Nu* values for Geometry 1.**

## Geometry 2 results

Figure 11 presents $Nu/Nu_0$ distributions obtained for Geometry 2 at around $Re_j$=15700 for the two investigated assemblies. Effusion holes locations and impingement holes projections are reported with the same notation of Figure 6.

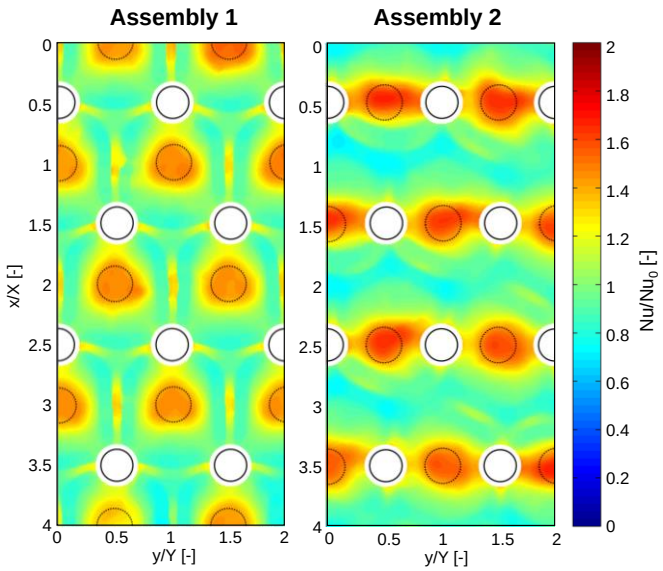


**Figure 11: $Nu/Nu_0$ distributions for Geometry 2 (I2E2) at around $Re_j$=15700.**

For this geometry, the shape of heat transfer pattern is strongly influenced by the presence and location of effusion holes. For the Assembly 1 a heat transfer peak is located below each impingement hole, as recorded for Geometry 1: in this case, however, the shape of such region is rather complex, with three distinct lobes directed towards the nearest effusion holes. This shape also extends to the surroundings of the stagnation region. Between adjacent jets, secondary high heat transfer regions can be observed, elongated in shape and perpendicular to a line linking the adjacent jet impact locations. These regions can be interpreted as a consequence of the fountain effect, which consists in the generation of two counter-rotating secondary vortices, as described by Cho and Rhee [2]. As schematized in Figure 12, a low heat transfer region is generated where the primary vortices detach from the wall, whereas the recirculation of the secondary vortices produces a sort of impingement effect, which results in an enhanced Nusselt number.

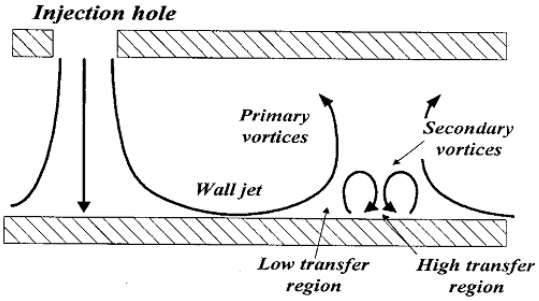


**Figure 12: Sketch of the "fountain effect" (Cho and Rhee [2])**

Assembly 2 also presents a *Nu* peak under each impingement jet, but its magnitude is significantly higher than the ones recorded for Assembly 1; moreover, the peak shape is deeply different, since it is elongated in the direction of the nearest effusion holes. Outside of such zones, low heat transfer regions are present in the areas between the effusion holes rows (x/X≈1, 2, 3). In fact, in these areas jet-jet interactions are weak and unstable: for Assembly 2, *Nu* peaks ascribable to fountain effect are located close to the lower side of the jets in the left side of the distribution (x/X < 1-1.5) and close to the upper side on the right side (x/X > 1-1.5). Multiple repetitions of the presented test show these regions to randomly migrate close to the higher or lower side of the jets. These considerations can be justified considering the lower distance between impingement and effusion holes, which results in a stronger interaction between the impingement jets and the coolant extraction, while far from the rows the lack of confinement induces the generation of flow unsteadiness. This phenomenon is inhibited for Assembly 1, where the coolant bleeding provided by effusion holes tends to stabilize this region, increasing at the same time the heat transfer. Overall, this effect compensates for the reduction of the peak value in the stagnation regions, giving an average $Nu/Nu_0$ of 1.07 for Assembly 1 and 1.08 for Assembly 2, hence resulting for the first configuration in roughly the same heat transfer entity, but a more homogeneous distribution. This conclusion is coherent with literature results (Cho and Rhee, [2]).

CFD simulations performed for Geometry 2 show also in this case a reasonable agreement, correctly reproducing the Nusselt number pattern in the region of stagnation (Figure 13). In the areas of jet-jet interactions, i.e. where the fountain effect occurs, the correct behaviour is still replicated, even though CFD solution shows higher gradients than observed experimentally. This discrepancy can be interpreted by considering that steady RANS approach returns a frozen solution of a highly unstable aero-thermal field, which inevitably smooths the measured data. This fact is particularly evident for the Assembly 2, where steady RANS solution omits the time evolution of the unsteady and randomly migrating jet-jet interaction regions and provides instead an ideal, instantaneous *Nu* pattern.

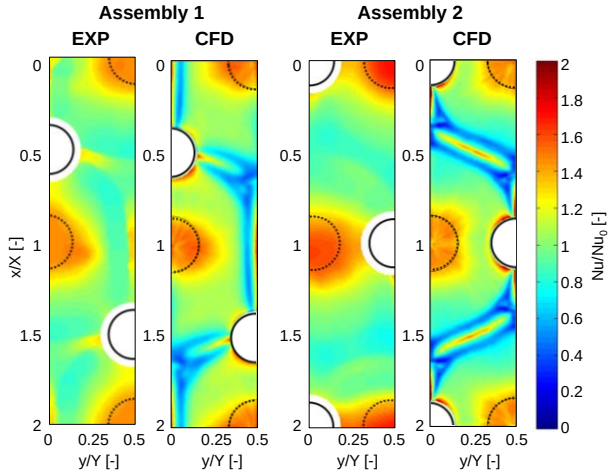


**Figure 13: *Nu/Nu₀* distributions for Geometry 2 (I2E2) at around *Re_j*=15700: comparison between experimental data and CFD simulations.**

The predicted flow fields depicted in Figure 14 clearly highlights a similarity with the sketch in Figure 12, with the formation of the primary and secondary vortices typical of fountain effect.

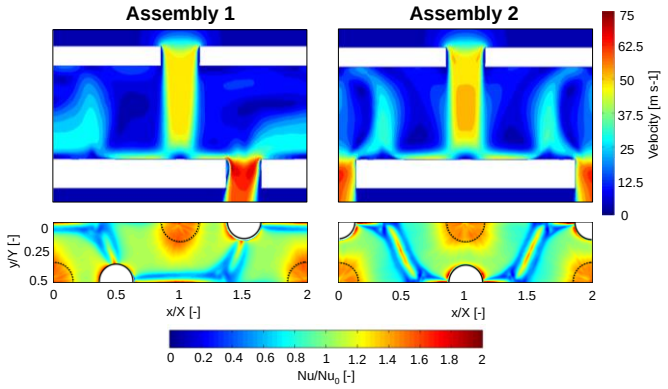


**Figure 14: Flow field predicted by CFD for Geometry 2 (I2E2) at around *Re_j*=15700.**

### Effect of coolant extraction

To evaluate the effect of coolant extraction in impingement heat transfer, Impingement 1 and 2 geometries (I1 and I2) have also been tested with a smooth target surface (E0). The results of such investigation are reported in Figure 15 and Figure 16, together with the corresponding *Nu/Nu₀* distributions obtained with effusion holes. The figures show the effect of coolant extraction is significantly different between the two geometries. For Impingement 1 (Figure 15) effusion holes seem not to dramatically alter the heat transfer pattern shape. However, if the distributions are analysed in closer detail, particular similarities can be identified for the first row (0<x/X<1) between I1E0 and I1E1-A1 configurations, since the peak region appears to be almost circular in shape and the peak is located directly under the impingement hole in both cases. For the I1E0 configuration the first row can be considered unaffected by the spent coolant flow (crossflow), which is directed towards the positive x direction: this fact confirms that effusion holes in Assembly 1 configuration do not significantly deflect the impingement jet. As a consequence, the main effect of coolant extraction consists in the higher peak *Nu/Nu₀* values: this can be due to a stabilizing effect of coolant extraction on the jet itself, which reduces spent coolant flow recirculation (Hollworth et al. [4]) and interaction with the free jet region and thus minimizes jet momentum losses, which in this case can play a significant role given the noticeable jet-to-target plate spacing ($Z/D_i$=6.5).

Evident similarities can also be identified for the third row (2<x/X<3) between I1E0 and I1E1-A2 configurations: in both cases, a slightly kidney-shaped *Nu/Nu₀* distribution is present near the jet impact location, and peak values are also similar.

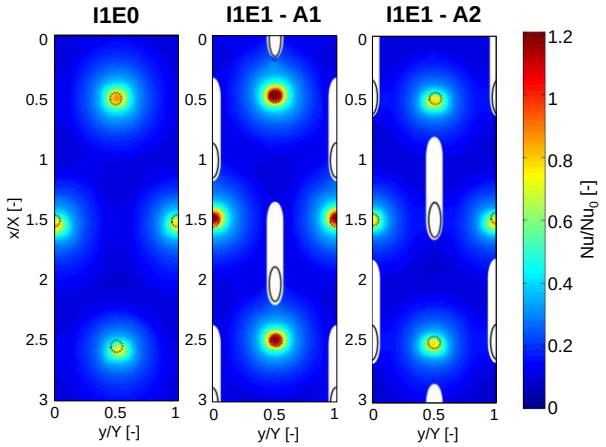


**Figure 15: *Nu/Nu₀* maps for Impingement 1 geometry (I1) at around *Re_j* = 7400.**

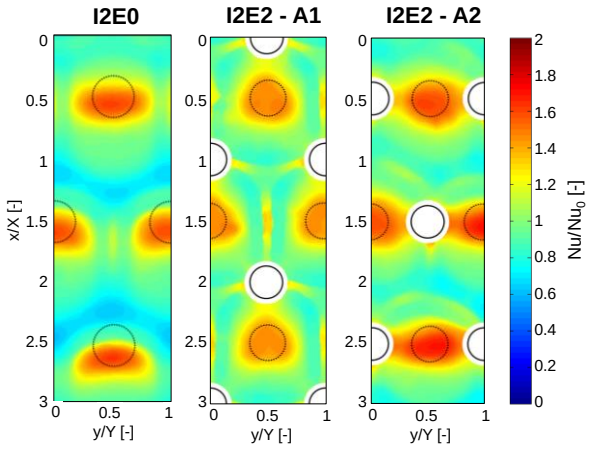


**Figure 16: *Nu/Nu₀* maps for Impingement 2 geometry (I2) at around *Re_j*=15700.**

For I1E0 configuration the crossflow generated by the first two rows of impingement holes impacts on the third one, deflecting the jets and decreasing heat transfer (Bailey and Bunker [16]); in the present case, the effect is slight due to the considerable jet-to-jet distances and height of impingement cavity. This fact however confirms the hypothesis, already highlighted by CFD results, that the lower values of A2 with respect to A1 are due to a local crossflow, induced by the effusion holes themselves.

For Impingement 2 (Figure 16), effusion holes have a significant effect on $Nu/Nu_0$ distribution shape. Without effusion holes (I2E0), $Nu/Nu_0$ peaks appear to be elongated in the y direction, and secondary peaks related to the fountain effect are present between adjacent holes of the same row (i.e. at the same x/X values). Given the low $X/D_i$, $Y/D_i$ and $Z/D_i$, crossflow is expected to be significant, and its main effects can be identified in the shape and the shift of the second and third rows peaks and in the evident decrease in peak $Nu/Nu_0$ values. The crossflow could also have prevented the development of secondary peaks between the jets of different rows (i.e. with different x/X values). If coolant extraction is considered, the positive effect of effusion holes can be observed, increasing secondary peak magnitude and thus heat transfer uniformity (I2E2-A1) or directly enhancing primary peaks (I2E2-A2).

Further considerations can be performed if area averaged $Nu/Nu_0$ values for the cases presented in Figure 15 and Figure 16 are considered (Figure 17): for the cases without effusion, Row 1 values are averaged over the area defined by $0<x/X<1$, Row 2 over $1<x/X<2$ and Row 3 over $2<x/X<3$, while for the sake of clarity area averaged values over the whole surface are reported for the cases with effusion (i.e. constant values of $Nu$ changing the Row number).

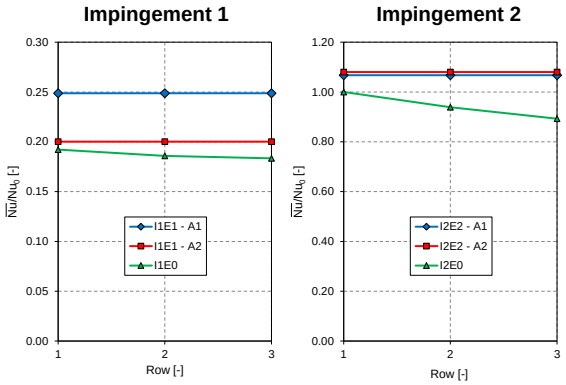


**Figure 17: Area averaged $Nu/Nu_0$ values for Impingement 1 and 2 with different target plates and assemblies**

For Impingement 1, the slight decrease of I1E0 values from Row 1 to Row 3 is due to the crossflow: with respect to this baseline case, I1E1-A1 presents area averaged values augmentations ranging from 29.4% (for Row 1) to 35.6% (for Row 3), while I1E1-A2 shows increases ranging from 4.2% (for Row 1) to 9.1% (for Row 3): the positive effect of coolant extraction is thus evident for A1 configuration, while comparable values are recorded for A2. It must be noticed that the effusion hole traces limit the optical access on the measurements surface and hence the area averaged showed in Figure 17 does not consider the entire target surface. However, as shown by CFD results, the effect of such approximation has been evaluated to decrease the area averaged values of around 7% in the worst case, thus the considerations reported above are still valid.

The results of I2 configurations show the sensibly stronger crossflow effect for the impingement only configuration (I2E0) with respect to I1, given the marked decrease of average $Nu/Nu_0$ values for Rows 1-3. The two configurations with effusion holes (I2E2-A1 and A2) seem to have a very similar behaviour, independently from the extraction hole assembly. If Row 1 values are considered, only a slight increase in heat transfer is registered if effusion holes are present (below 8%), while stronger increases are highlighted for Rows 2 and 3 (up to 21%): as a consequence, it can be stated that the positive effect of effusion holes for Impingement 2 is mainly due to the crossflow suppression.

## CONCLUSIONS

In the present work, two different impingement/effusion cooling systems have been investigated, with the aim to determine heat transfer distribution on the inner side of effusion wall. The geometries present the same number of impingement and effusion holes in staggered configurations, but with sparser (Geometry 1) and denser (Geometry 2) hole arrays. Two relative positions of impingement and effusion holes are investigated (Assembly 1 and 2), as well as the effect of Reynolds number and coolant extraction.

For Geometry 1, strong primary heat transfer peaks and small jet-jet interactions are recorded. In this case, the presence of effusion holes causes area averaged $Nu$ to increase up to 30% with respect to impingement only, with negligible alteration of heat transfer distribution shape: this has been interpreted as the effect of a reduction in the flow recirculation of spent coolant. For this geometry holes assembly is also important: by shifting the two assemblies of ½ holes pitch, reductions up to 33% in area averaged $Nu$ are obtained (at around $Re_j$=2500), due to the effusion holes flow field deflecting the impingement jets. The differences between the two investigated assemblies tend to decrease as $Re_j$ increases.

For Geometry 2, heat transfer appears to be strongly influenced by the presence and assembly of extraction holes. Assembly 1 presents a peculiar heat transfer distribution, with clover-shaped primary peaks under the impingement holes and strong secondary peaks midway between the jets induced by the fountain effect. Assembly 2 shows primary peaks elongated towards the two nearest effusion holes and with a higher magnitude with respect to Assembly 1, but also large regions of low and unstable heat transfer: this results in area averaged $Nu$ values similar to the ones of Assembly 1, but also in a less homogeneous distribution. With respect to impingement only configuration, significant heat transfer increases are recorded (around 15%), due to the suppression of the intense crossflow generated by the dense hole array.

The outcomes of the present work have shown that different geometries provide peculiar results: slight modifications to the cooling system can alter both shape and magnitude of heat transfer, due to the wide range of

parameters on which heat transfer depends and the strong interactions between different phenomena. Despite the limited number of investigated geometries, some general conclusions for impingement/effusion systems design can be provided:

- For sparse geometries ($X/D_i$ around 10, as Geometry 1) care should be taken so that the internal pressure field does not deflect the jets, thus maximizing heat transfer.
- For dense geometries ($X/D_i$ around 3, as Geometry 2) overall cooling performances show low sensibility to the impingement/effusion holes relative position (at least in the tested configurations): for this reason, the main concern is to avoid low heat transfer regions to occur, which can be obtained by making jets impinge in the region farthest from the effusion holes.
- CFD is a suitable tool for predicting fluid and thermal phenomena involved by an impingement/effusion system.

## NOMENCLATURE

| | | |
|---|---|---|
| $A$ | Area | $[m^2]$ |
| $D$ | Diameter | $[m]$ |
| $h$ | Convective heat transfer coefficient | $[W/m^2K]$ |
| $k$ | Thermal conductivity | $[W/mK]$ |
| $\dot{m}$ | Mass flow rate | $[kg/s]$ |
| $N$ | Holes number | [-] |
| $Nu$ | Nusselt number | [-] |
| $Re$ | Reynolds number | [-] |
| $S$ | Thickness | $[m]$ |
| $T$ | Temperature | $[K]$ |
| $t$ | Time | $[s]$ |
| $X$ | Jet-to-jet spacing ($x$ direction) | $[m]$ |
| $x$ | Streamwise direction | $[m]$ |
| $Y$ | Jet-to-jet spacing ($y$ direction) | $[m]$ |
| $y$ | Lateral direction | $[m]$ |
| $Z$ | Jet-to-target plate spacing | $[m]$ |

### Greeks

| | | |
|---|---|---|
| $\alpha$ | Thermal diffusivity | $[m^2/s]$ |
| $\beta$ | Angle with respect to plate | [°] |
| $\mu$ | Dynamic viscosity | $[Pa/s]$ |

### Subscripts

| | |
|---|---|
| 0 | Geometry 2 (impingement only), first row |
| $e$ | Effusion |
| $i$ | Impingement |
| $init$ | Initial |
| $j$ | Impingement jet |
| $w$ | Wall |

### Acronyms

| | |
|---|---|
| *CFD* | Computational Fluid Dynamics |
| *RANS* | Reynolds-Averaged Navier-Stokes |
| *TLC* | Thermochromic Liquid Crystal |

## REFERENCES


[1] Cho, H, and Goldstein, R, "Effect of hole arrangements on impingement/effusion cooling". In Proceedings of the 3rd KSME-JSME Thermal Engineering Conference, 1996, pp. 71–76.

[2] Cho, HH, and Rhee, DH, "Local heat/mass transfer measurement on the effusion plate in impingement/effusion cooling system". *Journal of turbomachinery*, *123*(3), 2000, pp.601–608

[3] Rhee, DH, Choi, JH, and Cho, HH, "Flow and heat (mass) transfer characteristics in an impingement/effusion cooling system with crossflow". *Journal of turbomachinery*, *125*(1), 2003, pp. 74–82.

[4] Hollworth, B, Lehmann, G, and Rosiczkowski, J, "Arrays of impinging jets with spent fluid removal through vent holes on the target surface, part 2: local heat transfer". *Journal of Engineering for Power*, *105*(2), 1983, pp. 393–402.

[5] Rhee, D-H, Yoon, P-H, and Cho, HH, "Local heat/mass transfer and flow characteristics of array impinging jets with effusion holes ejecting spent air". *International Journal of Heat and Mass Transfer*, *46*(6), 2003, pp. 1049– 1061.

[6] Hollworth, B, and Dagan, L, "Arrays of impinging jets with spent fluid removal through vent holes on the target surface part 1: Average heat transfer". *Journal of Engineering for Power*, *102*(4), 1980, pp. 994–999.

[7] Meyers, G, Van der Geest, J, Sanborn, J, and Davis, F, "Comparison of advanced cooling concepts using color thermography". In AIAA 3rd Applied Aerodynamics Conf. AIAA Paper AIAA-85, Vol. 1289, 1985.

[8] Cho, HH, Rhee, DH, and Goldstein, R, "Effects of hole arrangements on local heat/mass transfer for impingement/effusion cooling with small hole spacing". *Journal of turbomachinery*, *130*(4), 2008, 041003.

[9] Chan, TL, Ashforth-Frost, S, and Jambunathan, K, "Calibrating for viewing angle effect during heat transfer measurements on a curved surface". *International Journal of Heat and Mass Transfer*, *44*(12), 2001, pp. 2209–2223.

[10] Ireland, P, Wang, Z, and Jones, T, "Liquid crystal heat transfer measurements". *VKI Measurement and Techniques*, *1*, 1993.

[11] Camci, C, "Liquid crystal thermography". *In Temperature Measurements, Lecture Series 1996-07. von Karman Institute for Fluid Dynamics*, 1995.

[12] Vogel, G, and Weigand, B, "A new evaluation method for transient liquid crystal experiments". In National Heat Transfer Conf. NHTC2001-20250, California, 2001.

[13] ASME, "Measurement uncertainty". *In Instrument and apparatus, ANSI/ASME PTC 19.1-1985 of Performance Test Code*, 1985.

[14] Kline, SJ, and McClintock, FA, "Describing uncertainties in single sample experiments". *Mechanical Engineering*, *75*, 1953, pp. 3–8.

[15] Zuckerman, N, and Lior, N, "Jet impingement heat transfer: physics, correlations, and numerical modeling". *Advances in heat transfer*, *39*, 2006, pp. 565–631.

[16] Bailey, J, and Bunker, R, "Local heat transfer and flow distributions for impinging jet arrays of dense and sparse extent". In ASME Turbo Expo 2002: Power for Land, Sea, and Air, no. GT2002-30473, American Society of Mechanical Engineers, 2002, pp. 855–864. doi:10.1115/GT2002-30473.